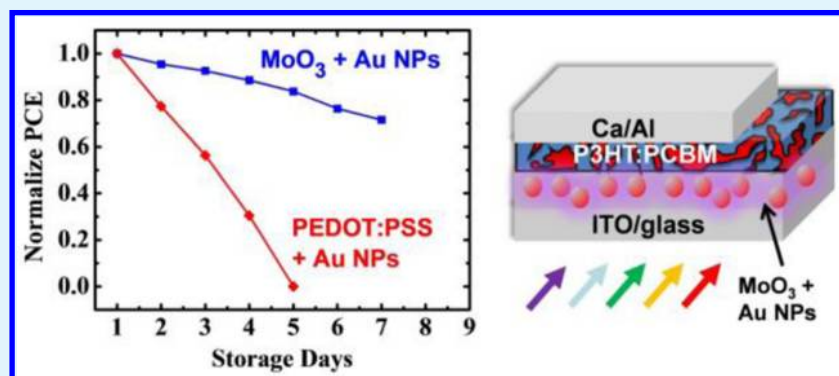# Solution-Processed Nanocomposites Containing Molybdenum Oxide and Gold Nanoparticles as Anode Buffer Layers in Plasmonic-Enhanced Organic Photovoltaic Devices

Kim-Shih Tan,[†] Ming-Kai Chuang,[†] Fang-Chung Chen,*,[†] and Chain-Shu Hsu[‡]

[†]Department of Photonics and Display Institute, National Chiao Tung University, Hsinchu 30010, Taiwan
[‡]Department of Applied Chemistry, National Chiao Tung University, Hsinchu 30010, Taiwan

S *Supporting Information*

ABSTRACT: Solution-processed nanocomposites containing molybdenum oxide (MoO_3) and gold nanoparticles (Au NPs) have been used as anode buffer layers in organic photovoltaic devices (OPVs). The resulting devices exhibit a remarkable enhancement in power conversion efficiency after Au NPs were incorporated into the device. Such enhancements can be attributed to the localized surface plasmon resonance induced by the metallic nanostructures. We have also found that the rate of exciton generation and the probability of exciton dissociation were increased. Furthermore, the devices made of the MoO_3 buffer layer containing Au NPs exhibited superior stability. This work opens up the possibility of fabricating OPVs with both high efficiency and a prolonged lifetime.

KEYWORDS: *molybdenum oxide, gold nanoparticles, plasmonic, polymer, photovoltaic devices, stability*

1. INTRODUCTION

Organic photovoltaic devices (OPVs) have been extensively studied because they have many advantageous properties, including low-cost fabrication, light weight, mechanical flexibility, and an amazing short period of energy pay-back time, compared to photovoltaic cells based on inorganic semiconductors.[1−4] Over the past few years, the efficiencies of OPVs have been improved substantially to over 10%.[4] Nevertheless, power conversion efficiency (PCE) of these devices still needs to be improved to compete with inorganic photovoltaic devices. Additionally, inferior operating stability is also a problem requiring emphatic concern.

Organic semiconductors usually exhibit low charge-carrier mobility and short exciton diffusion length. As a result, there exists a trade-off between light absorption and charge-collection efficiency in OPVs.[5,6] The thickness of the photoactive layer is limited largely to ∼100 nm for effective charge collection and reduced charge-recombination loss. To increase the absorption efficiency using thin films, many light-trapping approaches have been proposed.[5] For example, the introduction of a surface plasmon effect induced by metallic nanostructures[7] and the

incorporation of optical spacers for redistribution of the electrical field in the device[8,9] have been demonstrated successfully. Between these approaches, light trapping on the basis of localized surface plasmon resonance (LSPR) effects has received much attention as a means of improving the absorption efficiency.[7,10−17] Specifically, metal nanoparticles (NPs) are often introduced into the devices for triggering LSPRs. Their unique optical properties, including strong light scattering and local field enhancement, improve the absorption efficiency of OPVs substantially.

One simple method for incorporating the metal NPs into the devices is through doping soluble NPs in the anode buffer layers, such as poly(3,4-ethylenedioxythiophene):poly(styrene-sulfonate) (PEDOT:PSS).[12,13] The use of PEDOT:PSS, however, usually suffers from the problem of long-term stability because of its acidic and hygroscopic nature.[18] Alternatively, transition-metal oxides, such as molybdenum oxide (MoO_3)

and vanadium oxide (V_2O_5), can be used as an effective anode buffer layer for enhancing the charge-collection efficiency.[19−22] These metal oxides are usually fabricated through vacuum processes, which require higher cost. More recently, a simple, solution-processable method for synthesizing MoO_3 buffers has been reported using ammonium heptamolybdate $(NH_4)_6Mo_7O_{24}$-$4H_2O$ as a precursor.[22] The precursor was decomposed to MoO_3, resulting in an excellent buffer with high device performance comparable to that using PEDOT:PSS. Herein, we report one simple approach for preparing gold nanoparticles (AuNPs)/MoO_3 composites as the anode buffer layers of OPVs. The embedded Au NPs induced LSPR, which enhanced the local electromagnetic field of the active layer, thereby improving the device performance. The AuNP/MoO_3 nanocomposite layer is one of the most promising candidates for increasing the light-harvesting ability without significantly sacrificing the charge transport and/or collection efficiencies in OPVs. More importantly, the devices made of the MoO_3 buffer layer containing Au NPs exhibited superior stability. This work opens up the possibility of fabricating OPVs with both high efficiency and prolonged lifetime.

2. MATERIALS AND METHODS

2.1. Preparation of MoO_3 and AuNP/MoO_3 Thin Films. To prepare the MoO_3 solutions, ammonium heptamolybdate was dissolved in deionized water to form a 0.2 wt % solution.[22] The pH of the solution was adjusted to between 1 and 1.5. Then, the precursor solution was heated at 80 °C for 2 h in air. Ammonium heptamolybdate was decomposed to three components: MoO_3, NH_3, and H_2O.[22] Gaseous NH_3 was easily evaporated under the experimental conditions, and MoO_3 was left as the only solute in the solution. The Au NPs were synthesized following a procedure developed in a previous work.[23] Figure 1b displays the scanning
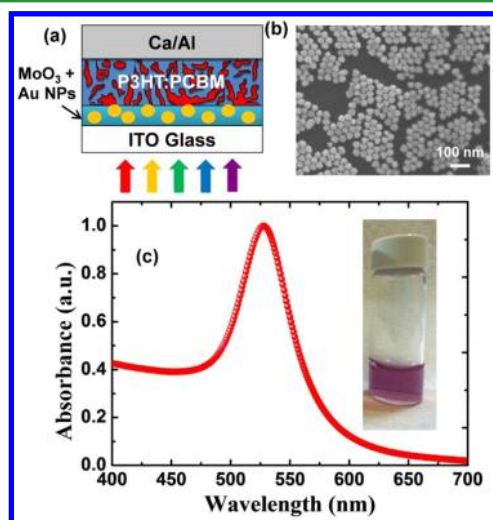
Figure 1. (a) Device structure of the OPVs in this study. (b) SEM image of the Au NPs. The average size was 40 ± 5 nm. (c) UV−vis absorption spectrum of the Au NPs suspended in water. The inset shows a photograph of the Au NP solution.

electron microscopy (SEM) image of the octahedral Au NPs. We observed that the average particle size of the Au NPs was approximately 40 nm.[17] For the preparation of the composite buffer layers, the Au NPs were mixed with the as-prepared MoO_3 solution (Figure 2a). The anode buffer layers were prepared by spin coating the aqueous mixtures containing both Au NPs and MoO_3 precursors onto the UV−O_3-pretreated indium tin oxide (ITO)-coated glass substrates. The samples were annealed at 150 °C for 10 min in air. Figure 2b
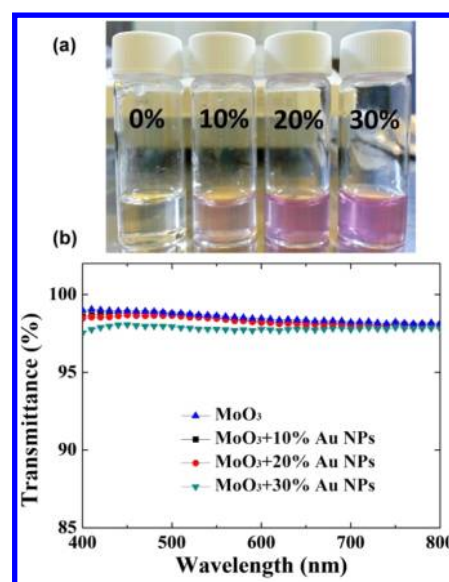
Figure 2. (a) Photograph of the MoO_3 solution containing various volume ratios of Au NPs for preparing the anode buffer layers. (b) Transmittance spectra of the MoO_3 thin films deposited on ITO glass substrates. Different concentrations of Au NPs were embedded in the thin films.

reveals the transmittance spectra of the MoO_3 solution incorporating Au NPs with different concentrations. We can see that the neat MoO_3 film exhibited high transmittance in the visible spectral region. Because the plasmon band of Au NPs was around 530 nm, the transmittance decreased upon the addition of Au NPs.

2.2. Fabrication of Photovoltaic Devices. The devices were fabricated on ITO-coated glass substrates. The device structure in this work is illustrated in Figure 1a. The ITO substrates were treated with UV-ozone prior to use. The Au NP/MoO_3 films were prepared using spin coating as described above. The photoactive layer comprising regioregular poly(3-hexylthiophene) (P3HT) and 1-(3-methoxycarbonyl)propyl-1-pheny[6,6]methanofullerene (PCBM) at a weight ratio of 1:1 was spin-coated from a solution of 1,2-dicholorobenzene on the anode buffer layers. After solvent annealing,[24,25] the dried film was further annealed at 110 °C for 10 min. The resulting thickness of the active layer was ∼180 nm. Finally, the metals Ca (30 nm) and Al (100 nm) were thermally evaporated sequentially to form the cathodes. The device active area was 0.1 cm^2. The thickness of the MoO_3 buffer layers was ca. 10 nm.

2.3. Characterization. For the device characteristics, a Keithley 2400 source measure unit was used for recording the current density−voltage ($J−V$) curves. The electrical properties of the devices under illumination conditions were measured using a 150 W Thermal Oriel solar simulator equipped with standard AM 1.5G filters. The light intensity of the simulator was further calibrated using a Si photodetector containing a KG5 filter.[26] The incident photon-to-electron conversion efficiency (IPCE) curves were obtained from a measurement system (Enli Technology) composed of a quartz-tungsten-halogen lamp, a monochromator, an optical chopper, a lock-in amplifier, and a calibrated silicon-based diode.

3. RESULTS AND DISCUSSION

Figure 3 displays the $J−V$ characteristics of the devices fabricated with various amounts of Au NPs; the measurements were performed under standard illumination conditions (AM 1.5G, 100 mW cm$^{−2}$). The controlled device, in which a layer of pristine MoO_3 was used as the anode buffer, exhibited an open-circuit voltage (V_{oc}) of 0.60 V, a short-circuit current (J_{sc}) of 10.2 mA cm$^{−2}$, and a fill factor (FF) of 0.60. The calculated PCE was 3.68%. The results were consistent with those
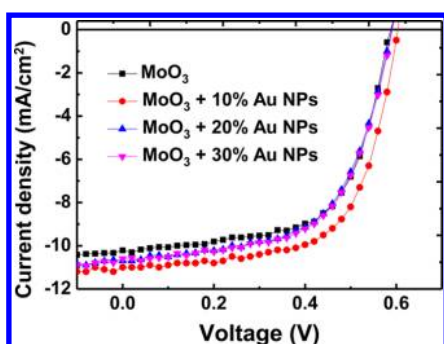
Figure 3. $J-V$ characteristics obtained under AM 1.5G illumination (100 mW cm^{-2}) of the OPVs prepared with MoO$_3$ layers incorporating various amounts of Au NPs.

Figure 4. (a) IPCE spectra for the photovoltaic devices prepared with various concentrations of Au NP solutions. (b) Increase in IPCE (ΔIPCE) after the use 10% Au NPs in the anode buffer layer and the absorption spectrum of the Au NPs. The absorption spectrum was obtained using a neat MoO$_3$ thin film as the baseline.

reported previously.[22] After the incorporation of Au NPs to the MoO$_3$ buffer layer, the photocurrent and *FF* were improved. For the optimized device, the J_{sc} and *FF* values were improved to 10.9 mA cm^{-2} and 0.65, respectively. The values of V_{oc} remained unchanged (0.60 V), indicating that the anode interface was not significantly affected by the Au NPs. As a result, the PCE was increased to 4.20%. We also extracted the device series resistance (R_s) from the $J-V$ curves measured in the dark (Figure S1). The values of R_s increased from 1.7 to 1.9 Ω cm^2 after the addition of 10% Au NPs, suggesting that the device improvement was not due to the reduction in device resistance. Rather, the advantageous LSPR effect induced by the Au NPs overwhelmed the inferior electrical properties of the devices containing Au NPs.[17] We also note that a further increase in the amount of the Au NPs resulted in a decrease in the value of J_{sc}. We suspected that the excess Au NPs might lead to enhanced backward scattering. Furthermore, the high concentration of NPs might also increase the resistivity of the buffer layers. From the $J-V$ curves measured in the dark, we indeed obtained an increased R_s to 2.4 Ω cm^2 after the addition of 30% Au NPs. Table 1 summarizes the device performance in this work.

Figure 4a shows the IPCE spectra of the solar cells prepared with different anode buffers. We can see that the trends in the IPCE were consistent with those for the values of J_{sc}. The devices containing Au NPs exhibited higher efficiencies. Furthermore, we also noted that the spectral shape changed after the use of Au NP solutions. The efficiencies increased substantially within the spectral range from 450 to 600 nm. The peak efficiency was improved to 66% at 550 nm for the device containing 10% Au NPs. Figure 4b displays the corresponding curve of the increase in IPCE (ΔIPCE) for the solar cell containing 10% Au NPs; the extinction spectrum of the Au NPs is also included in Figure 4b for comparison. The spectral regime in which the IPCE values were increased was matched with the plasmonic band of the Au NPs. The spectral
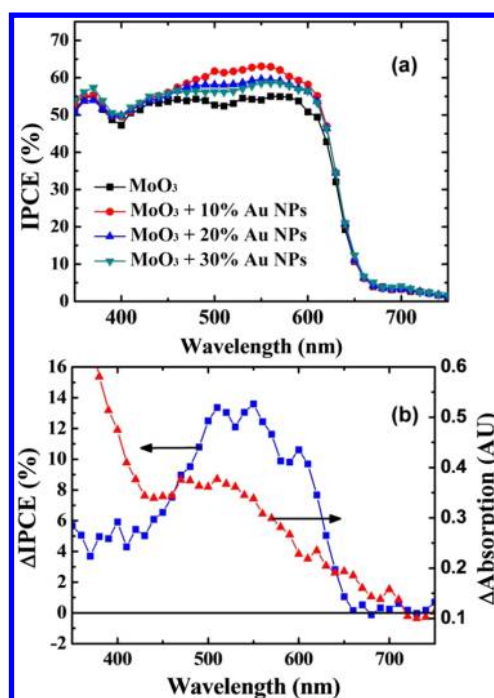
consistence suggested that the LSPR contributed to the device enhancement.

The morphology changes of the MoO$_3$:Au NP layer were investigated using atomic force microscopy (AFM), and the topographic images are displayed in Figure 5. The root-mean-square (rms) roughness of the MoO$_3$ film was 8.8 nm (Figure 5a). Upon the addition of Au NPs, we observed obvious changes in the surface morphology of the MoO$_3$ films. The rms roughness was increased to 10.4, 11.9, and 12.7 nm after the incorporation of 10, 20, and 30% of Au NP solutions, respectively. The rough surface might induce trap states at the interfaces and somehow affect the charge-transport/collection efficiencies of the OPVs, resulting in a lower photocurrent. The increased R_s value of the devices containing 20 and 30% Au NPs further confirmed this assumption. For the device containing 10% Au NPs, however, the drawback of the poor interfaces was overwhelmed by the higher degree of absorption upon the addition of Au NPs, thereby improving the overall device PCE.

The transmission electron microscopy (TEM) image of the MoO$_3$ containing 10% Au NP solution was obtained to study further the morphology of the thin films (Figure S2). We observed large particles, which might be due to the formation of MoO$_3$. However, the dark dots should be Au NPs in the

Table 1. Electrical Characteristics of Devices Incorporating Various Amounts of Au NPs

concentration of Au NPs (%)	V_{oc} (V)	J_{sc} (mA cm^{-2})	*FF*	PCE (%)	R_s (Ω cm^2)[a]
0	0.60 ± 0.01	10.2 ± 0.17	0.60 ± 0.02	3.68 ± 0.08	1.7 ± 0.1
10	0.60 ± 0.01	10.9 ± 0.20	0.64 ± 0.02	4.20 ± 0.11	1.9 ± 0.1
20	0.60 ± 0.01	10.7 ± 0.25	0.62 ± 0.03	3.97 ± 0.12	2.1 ± 0.2
30	0.60 ± 0.01	10.6 ± 0.21	0.61 ± 0.02	3.86 ± 0.10	2.4 ± 0.1

[a]Device series resistance (R_s) was obtained from the inverse slope of the dark $J-V$ curve.
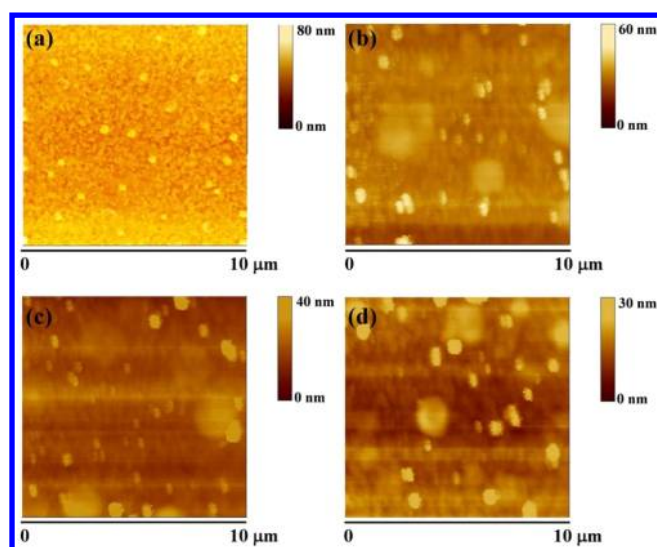
Figure 5. AFM images ($10 \times 10~\mu m^2$) of the MoO_3 buffer layers prepared with different concentrations of Au NP solutions: (a) 0, (b) 10, (c) 20, and (d) 30% Au NP solution doping.

nanocopposites, which did not aggregate in the thin films. The results suggest that the rougher surface, as revealed in the AFM images, could be due to the aggregation of MoO_3 particles.

The photocurrent behavior of the plasmonic-enhanced device was further investigated to study the LSPR effects on the device performance. Through the calculation of the maximum generation rate (G_{max}), we were able to evaluate the overall light harvesting. The devices were biased swept from +1 to −10 V under 100 mW cm^{-2} illumination (AM 1.5G). Figure 6a displays the dependence of the photocurrent (J_{ph}) on the effective applied voltage (V_{eff}). The photocurrent accounts for the dark current (J_D) using the equation[27,28]

Figure 6. (a) Plots of photocurrent density as a function of the effective bias for devices prepared with neat MoO_3 and MoO_3 containing 10% Au NP solution. (b) Exciton dissociation probability $[P(E,T)]$ plotted with respect to V_{eff} for the device prepared with and without Au NPs.

$$J_{ph} = J_L - J_D \tag{1}$$

where J_L is the measured current density under illumination. Furthermore, V_{eff} was calculated according to the equation

$$V_{eff} = V_o - V_a \tag{2}$$

where V_o is the voltage, the value of J_{ph} equals zero (i.e., $J_L = J_D$), and V_a is the applied bias on the devices. From Figure 6a, we can clearly see two different regimes. In the first, J_{ph} linearly increases with the increasing V_{eff}. Then, J_{ph} becomes saturated at a sufficiently high value of V_{eff}. We determined the value of such a photocurrent at high biases to be the saturation photocurrent density (J_{sat}), which should be theoretically independent of the applied electrical field and temperature.[27,28] Under the saturation conditions, all of the excitons generated in the device could be dissociated and contributed to the current owing to the high electric potential, which could overcome the exciton binding energy. Therefore, we express J_{sat} as

$$J_{sat} = qG_{max}L \tag{3}$$

where q is the electronic charge and L is the thickness of the active layer.[27,28] Therefore, the maximum exciton generation rate (G_{max}) can be calculated from the measured results of J_{sat}. Because the value of G_{max} is relative to the maximum number of photons absorbed in the devices, it can be considered as one key parameter for evaluating the absorption ability of typical OPVs. From Figure 6a, the values of G_{max} were 3.82×10^{27} and 4.13×10^{27} m^{-3} s^{-1} for the device prepared without and with Au NPs, respectively. The noticeable increase in G_{max} for the device containing the Au NPs suggests an enhanced light-harvesting ability of the plasmonic device.
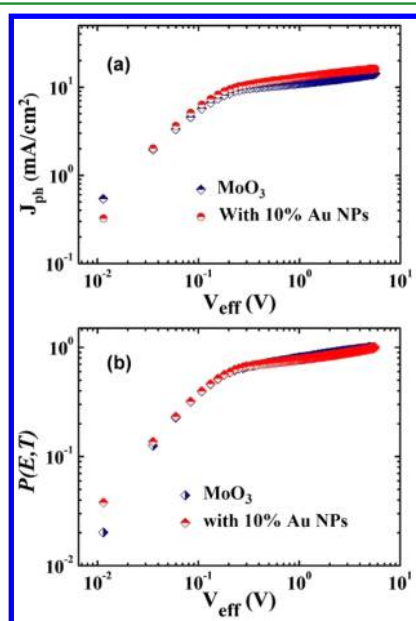
Furthermore, the exciton dissociation probabilities $[P(E,T)]$ were also affected by the LSPR.[13] For OPVs, only a portion of the exciton can be dissociated into free carriers under normal operation conditions. Therefore, J_{ph} can be expressed as the following equation[27,28]

$$J_{ph} = qG_{max}(E, T)L \tag{4}$$

Assuming the dissociation probability is 100% under saturation conditions, the value of $P(E,T)$ under various bias conditions can be calculated from the plot of the normalized photocurrent density (J_{ph}/J_{sat}). Figure 6b displays the normalized photocurrent density. Under the short-circuit conditions ($V_a = 0$ V), the result indicates that the probability of $P(E,T)$ was increased from 78.7 to 84.9% for the device incorporating 10% AuNPs. We infer that excitation of the LSPR could also facilitate exciton dissociation, increasing the photocurrent of the plasmonic devices.

From the device results, we also noted that FF values were increased after the use of Au NPs. In fact, a higher exciton dissociation probability decreases the recombination rate.[13] Furthermore, the device series resistance was increased slightly, suggesting that the improvement in the FF values was not due to the reduction of resistance. Therefore, we suggest that the LSPR effects increased the exciton dissociation probability, thereby increasing the FF values.[13]

The results of steady-state photoluminescence (PL) measurements of the P3HT:PCBM thin films prepared on various buffer layers also helped to understand the LSPR effect on the exciton generation behavior; Figure 7 shows the PL results. The peak intensity of the thin film containing Au NPs apparently became higher by approximately 60%. As was noted previously, because of the good overlap between the resonance
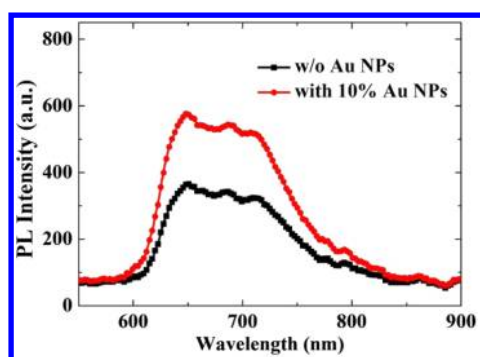
Figure 7. Photoluminescent spectra of the P3HT:PCBM thin films deposited on the MoO₃ layers prepared with and without Au NPs. A 470 nm laser was used as the excitation source.

peak of the Au NPs and the absorption spectrum of P3HT, we attributed the increased PL intensity to the increased level of photon absorption. The enhanced PL intensity probably arises from the coupling between the plasmonic field of the Au NPs and the excited state of P3HT.

The long-term stability of devices was investigated by testing the shelf lifetime. The solar cells were stored under ambient conditions in which the relative humidity during the period of measurement was controlled at ca. 60%. The test protocols could be qualified as an ISOS-D-1 experiment.[29] Figure 8 shows
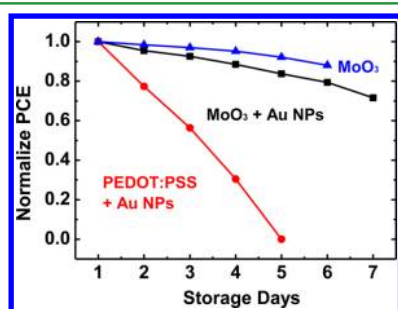
Figure 8. Normalized PCEs of devices fabricated with PEDOT:PSS or MoO₃ anode buffer layers plotted as a function of time. Au NPs were incorporated into the buffer layers. The devices, which were not encapsulated, were stored under ambient conditions.

the normalized PCEs of the devices as a function of time. It can be seen that the device made of a PEDOT:PSS buffer layer degraded much more rapidly. The PCE decreased to 50% of the initial efficiency within the first 3 days. No apparent electrical response could be measured after 5 days. In contrast, the devices fabricated with MoO₃ buffer layers exhibited higher stability. The addition of Au NPs slightly affects the device stability, which is probably due to the degradation of the interface as the surface of the buffer layer becomes rougher (Figure 5).[30] For the device containing 10% Au NPs, however, the PCE still remained at ca. 80% of its initial value after storing the device for 7 days. The replacement of the hygroscopic PEDOT:PSS with MoO₃ might reduce the diffusion rate of humidity within the devices, thus reducing the degree of oxidation of the cathode. Furthermore, unlike the acidic PEDOT:PSS, the MoO₃ buffer could also avoid the corrosion of the ITO anode.

4. CONCLUSIONS

We have developed a simple, solution-processed method for preparing oxide buffer layer containing Au NPs for OPVs. The plasmonic effects induced by the Au NPs enhanced the photocurrent and PCE of the devices. More importantly, the devices fabricated with these Au NP/MoO₃ buffer layer exhibited a longer device lifetime. We foresee that the metal/oxide nanocomposites reported herein might be of further use in other material systems, such as low-band-gap polymers, to achieve even higher efficiencies and prolonged stability.

■ ASSOCIATED CONTENT

Ⓢ Supporting Information

$J-V$ characteristics of the devices measured in the dark, and TEM image of the nanocomposites. This material is available free of charge via the Internet at http://pubs.acs.org.

■ AUTHOR INFORMATION

Corresponding Author
*E-mail: fcchen@mail.nctu.edu.tw.
Notes
The authors declare no competing financial interest.

■ ACKNOWLEDGMENTS

■ REFERENCES

(1) Yip, H. L.; Jen, A. K.-Y. *Energy Environ. Sci.* **2012**, *5*, 5994−6011.
(2) Servaites, J. D.; Ratner, M. A.; Marks, T. J. *Energy Environ. Sci.* **2011**, *4*, 4410−4422.
(3) Roes, A. L.; Alsema, E. A.; Blok, K.; Patel, M. K. *Prog. Photovoltaics* **2009**, *17*, 372−393.
(4) Li, G.; Zhu, R.; Yang, Y. *Nat. Photonics* **2012**, *6*, 153−161.
(5) Ko, D. H.; Tumbleston, J. R.; Gadisa, A.; Aryal, M.; Liu, Y.; Lopez, R.; Samulski, E. T. *J. Mater. Chem.* **2011**, *21*, 16293−16303.
(6) Park, S. H.; Roy, A.; Beaupre, S.; Cho, S.; Coates, N.; Moon, J. S.; Moses, D.; Leclerc, M.; Lee, K.; Heeger, A. J. *Nat. Photonics* **2009**, *3*, 297−302.
(7) Gan, Q.; Bartoli, F. J.; Kafafi, Z. H. *Adv. Mater.* **2013**, *25*, 2385−2396.
(8) Kim, J. Y.; Kim, S. H.; Lee, H.-H.; Lee, K.; Ma, W.; Gong, X.; Heeger, A. J. *Adv. Mater.* **2006**, *18*, 572−576.
(9) Chen, F. C.; Wu, J.- L.; Hung, Y. *Appl. Phys. Lett.* **2010**, *96*, 193304-1−193304-3.
(10) Wang, D. H.; Park, K. H.; Seo, J. H.; Seifter, J.; Jeon, J. H.; Kim, J. K.; Park, J. H.; Park, O. O.; Heeger, A. J. *Adv. Energy Mater.* **2011**, *1*, 766−770.
(11) Li, X.; Choy, W. C. H.; Lu, H.; Sha, W. E. I.; Ho, A. H. P. *Adv. Funct. Mater.* **2013**, *21*, 2728−2735.
(12) Chen, F. C.; Wu, J.-L.; Lee, C. L.; Hong, Y.; Kuo, C. H.; Huang, M. H. *Appl. Phys. Lett.* **2009**, *95*, 013305-1−013305-3.
(13) Wu, J. L.; Chen, F. C; Hsiao, Y. S.; Chien, F. C.; Chen, P.; Kuo, C. H.; Huang, M. H.; Hsu, C. S. *ACS Nano* **2011**, *5*, 959−967.
(14) Yang, X.; Chueh, C. C.; Li, C. Z.; Yip, H. L.; Yin, P.; Chen, H.; Chen, W. C.; Jen, A. K. Y. *Adv. Energy Mater.* **2013**, *3*, 666−673.
(15) Baek, S. W.; Noh, J.; Lee, C. H.; Kim, B.; Seo, M. K.; Lee, J. Y. *Sci. Rep.* **2013**, *3*, 1726.
(16) Hsiao, Y. S.; Charan, S.; Wu, F. Y.; Chien, F. C; Chu, C. W.; Chen, P.; Chen, F. C *J. Phys. Chem. C* **2012**, *116*, 20731−20737.

(17) Kao, C. S.; Chen, F. C; Liao, C. W.; Huang, M. H.; Hsu, C. S. *Appl. Phys. Lett.* **2012**, *101*, 193902-1−193902-4.

(18) Jórengsen, M.; Norrman, K.; Krebs, F. C. *Sol. Energy Mater. Sol. Cells* **2008**, *92*, 686−714.

(19) Shrotriya, V.; Li, G.; Yao, Y.; Chu, C. W.; Yang, Y. *Appl. Phys. Lett.* **2006**, *88*, 073508-1−073508-3.

(20) Sun, Y.; Takacs, C. J.; Cowan, S. R.; Seo, J. H.; Gong, X.; Roy, A.; Heeger, A. J. *Adv. Mater.* **2011**, *23*, 2226−2230.

(21) Yang, T.; Wang, M.; Cao, Y.; Huang, F.; Huang, L.; Peng, J.; Gong, X.; Cheng, S. Z. D.; Cao, Y. *Adv. Energy Mater.* **2012**, *2*, 523−527.

(22) Murase, S.; Yang, Y. *Adv. Mater.* **2012**, *24*, 2459−2462.

(23) Chang, C. C.; Wu, H. L.; Kuo, C. H.; Huang, M. H. *Chem. Mater.* **2008**, *20*, 7570−7574.

(24) Li, G.; Yao, Y.; Yang, H.; Shrotriya, V.; Yang, G.; Yang, Y. *Adv. Funct. Mater.* **2007**, *17*, 1636−1644.

(25) Chen, F. C.; Ko, C. J.; Wu, J. L.; Chen, W. C. *Sol. Energy Mater. Sol. Cells* **2010**, *94*, 2426−2430.

(26) Shrotriya, V.; Li, G.; Yao, Y.; Moriarty, T.; Emery, K.; Yang, Y. *Adv. Funct. Mater.* **2006**, *16*, 2016−2023.

(27) Mihailetchi, V. D.; Koster, L. J. A.; Hummelen, J. C.; Blom, P. W. M. *Phys. Rev. Lett.* **2004**, *93*, 216601-1−216601-4.

(28) Mihailetchi, V. D.; Xie, H. X.; de Boer, B.; Koster, L. J. A.; Blom, P. W. M. *Adv. Funct. Mater.* **2006**, *16*, 699−708.

(29) Reese, M. O.; Gevorgyan, S. A.; Jørgensen, M.; Bundgaard, E.; Kurtz, S. R.; Ginley, D. S.; Olson, D. C.; Lloyd, M. T.; Morvillo, P.; Katz, E. A.; Elschner, A.; Haillant, O.; Currier, T. R.; Shrotriya, V.; Hermenau, M.; Riede, M.; Kirov, K. R.; Trimmel, G.; Rath, T.; Inganas, O.; Zhang, F.; Andersson, M.; Tvingstedt, K.; Lira-Cantu, M.; Laird, D.; McGuiness, C.; Gowrisanker, S. (J.); Pannone, M.; Xiao, M.; Hauch, J.; Steim, R.; DeLongchamp, D. M.; R€osch, R.; Hoppe, H.; Espinosa, N.; Urbina, A.; Yaman-Uzunoglu, G.; Bonekamp, J.-B.; van Breemen, A. J. J. M.; Girotto, C.; Voroshazi, E.; Krebs, F. C. *Sol. Energy Mater. Sol. Cells* **2011**, *95*, 1253−1267.

(30) Chen, F. C.; Chien, S. C. *J. Mater. Chem.* **2009**, *19*, 6865−6869.